



1 **Impacts of aerosol-photolysis interaction and aerosol-radiation**
2 **feedback on surface-layer ozone in North China during a multi-**
3 **pollutant air pollution episode**

4

5 Hao Yang¹, Lei Chen¹, Hong Liao¹, Jia Zhu¹, Wenjie Wang², Xin Li²

6

7 ¹Jiangsu Key Laboratory of Atmospheric Environment Monitoring and Pollution
8 Control, Jiangsu Collaborative Innovation Center of Atmospheric Environment and
9 Equipment Technology, School of Environmental Science and Engineering, Nanjing
10 University of Information Science & Technology, Nanjing 210044, China

11 ²State Joint Key Laboratory of Environmental Simulation and Pollution Control,
12 College of Environmental Sciences and Engineering, Peking University, Beijing
13 100871, China

14

15 **Correspondence:** Lei Chen (chenlei@nuist.edu.cn) and Hong Liao
16 (hongliao@nuist.edu.cn)

17



18 Abstract

19 We examined the impacts of aerosol-radiation interactions, including the effects of
20 aerosol-photolysis interaction (API) and aerosol-radiation feedback (ARF), on surface-
21 layer ozone (O_3) concentrations during one multi-pollutant air pollution episode
22 characterized by high O_3 and $PM_{2.5}$ levels from 28 July to 3 August 2014 in North China,
23 by using the Weather Research and Forecasting with Chemistry (WRF-Chem) model
24 embedded with an integrated process analysis scheme. Our results show that aerosol-
25 radiation interactions decrease the daytime downward shortwave radiation at surface, 2
26 m temperature, 10 m wind speed, planetary boundary layer height, photolysis rates
27 $J[NO_2]$ and $J[O^1D]$ by 115.8 W m^{-2} , $0.56 \text{ }^\circ\text{C}$, 0.12 m s^{-1} , 129 m, $1.8 \times 10^{-3} \text{ s}^{-1}$ and $6.1 \times$
28 10^{-6} s^{-1} , and increase relative humidity at 2 m and downward shortwave radiation in the
29 atmosphere by 2.4% and 72.8 W m^{-2} . The weakened photolysis rates and changed
30 meteorological conditions reduce surface-layer O_3 concentrations by up to 11.4 ppb
31 (13.5%), with API and ARF contributing 74.6% and 25.4% of the O_3 decrease,
32 respectively. The combined impacts of API and ARF on surface O_3 are further
33 quantitatively characterized by the ratio of changed O_3 concentration to local $PM_{2.5}$
34 level. The ratio is calculated to be $-0.14 \text{ ppb } (\mu\text{g m}^{-3})^{-1}$ averaged over the multi-pollutant
35 air pollution area in North China. Process analysis indicates that the weakened O_3
36 chemical production makes the greatest contribution to API effect while the reduced
37 vertical mixing is the key process for ARF effect. This study implies that future $PM_{2.5}$
38 reductions will lead to O_3 increases due to weakened aerosol-radiation interactions.
39 Therefore, tighter controls of O_3 precursors are needed to offset O_3 increases caused by
40 weakened aerosol-radiation interactions in the future.

41



42 **1 Introduction**

43 China has been experiencing severe air pollution in recent years, characterized by
44 high loads of PM_{2.5} (particulate matter with an aerodynamic equivalent diameter of 2.5
45 micrometers or less) and high levels of ozone (O₃). Observational studies exhibited
46 positive correlations and synchronous occurrence of PM_{2.5} and O₃ pollution in North
47 China during summer (Zhao et al., 2018; Zhu et al., 2019), indicating that complex air
48 pollution is becoming a major challenge for North China.

49 Aerosols can absorb and scatter solar radiation and therefore alter radiative balance.
50 They can also act as cloud condensation nuclei and ice nuclei, and further modify the
51 microphysical characteristics of clouds (Albrecht et al., 1989; Haywood et al., 2000;
52 Lohmann et al., 2005). Both ways perturb meteorological variables, e.g., temperature,
53 planetary boundary layer height (PBLH), and precipitation, and eventually influence
54 air pollutants (Petäjä et al., 2015; Miao et al., 2018; Zhang et al., 2018). Many studies
55 were focused on the feedback between aerosol and meteorology (Gao et al., 2015; Gao
56 et al., 2016a; Qiu et al., 2017; Chen et al., 2019; Zhu et al., 2021). Gao et al. (2015)
57 pointed out that aerosols could cause a decrease in surface temperature by 0.8-2.8 °C
58 but an increase of 0.1-0.5 °C around 925 hPa when feedbacks between aerosols and
59 meteorological variables were considered in WRF-Chem model. The more stable
60 atmosphere caused by surface cooling and higher-layer heating led to the decreases of
61 surface wind speed and PBLH by 0.3 m s⁻¹ and 40-200 m, respectively, which further
62 resulted in overall PM_{2.5} increases by 10-50 µg m⁻³ (2-30%) over Beijing, Tianjin and
63 south Hebei during January 2013. By using the same WRF-Chem model, Qiu et al.
64 (2017) reported that the surface downward shortwave radiation and PBLH were
65 reduced by 54.6 W m⁻² and 111.4 m due to aerosol radiative forcing during 21 and 27
66 February 2014 in North China Plain. As a result, the PM_{2.5} concentration averaged over
67 the North China Plain was increased by 34.9 µg m⁻³ (20.4%).

68 Aerosols can also influence O₃ through aerosol-radiation interactions, including
69 aerosol-photolysis interaction and aerosol-radiation feedback. Aerosols can scatter and
70 absorb UV radiation, and therefore directly affect O₃ photochemistry reactions, which



71 is called aerosol-photolysis interaction (API) (Dickerson et al., 1997; Liao et al., 1999;
72 Li et al., 2011; Lou et al., 2014). The changed meteorological variables due to aerosol
73 radiative forcing can indirectly affect O₃ concentrations, which is called aerosol-
74 radiation feedback (ARF) (Hansen et al., 1997; Gao et al., 2018; Liu et al., 2020).
75 Although the effects of API or ARF on O₃ have been examined by previous studies
76 (Xing et al., 2017; Gao et al., 2018; Gao et al., 2020), the combined effects of API and
77 ARF on O₃, especially under the conditions of synchronous occurrence of high PM_{2.5}
78 and O₃ concentrations, remain largely elusive.

79 The present study aims to (1) quantify the respective/combined contributions of
80 API and ARF on O₃ concentrations by using the WRF-Chem model; (2) explore the
81 prominent physical and/or chemical processes responsible for API and ARF effects by
82 using an integrated process rate (IPR) analysis embedded in WRF-Chem model. The
83 analysis is conducted during one multi-pollutant air pollution episode characterized by
84 high O₃ and PM_{2.5} levels from 28 July to 3 August 2014 in North China. The model
85 configuration, numerical experiments, observational data, and the integrated process
86 rate analysis are described in section 2. Section 3 shows the model evaluation. The
87 presentation and discussion of the model results are exhibited in section 4, and the
88 conclusion is provided in section 5.

89 **2 Methods**

90 **2.1 Model configuration**

91 The version 3.7.1 of the online-coupled Weather Research and Forecasting with
92 Chemistry (WRF-Chem) model (Grell et al., 2005; Skamarock et al., 2008) is used in
93 this study to explore the impacts of aerosol-radiation interactions on surface-layer O₃
94 in North China. WRF-Chem can simulate gas phase species and aerosols coupled with
95 meteorological fields, and has been widely used to investigate air pollution over North
96 China (Gao et al., 2016a; Gao et al., 2020; Wu et al., 2020). As shown in Fig. 1, we
97 design two nested model domains with the number of grid points of 57 (west–east) ×
98 41 (south–north) and 37 (west–east) × 43 (south–north) at 27 and 9 km horizontal
99 resolutions, respectively. The parent domain centers at 39 °N, 117 °E. The model



100 contains 29 vertical levels from the surface to 50 hPa, with 14 levels below 2 km for
101 the fully description of the vertical structure of planetary boundary layer (PBL).

102 The Carbon Bond Mechanism Z (CBM-Z) is selected as the gas-phase chemical
103 mechanism (Zaveri and Peters, 1999), and the full 8-bin MOSAIC (Model for
104 Simulating Aerosol Interactions and Chemistry) aerosol module with aqueous
105 chemistry is used to simulate aerosol evolution (Zaveri et al., 2008). The photolysis
106 rates are calculated by the Fast-J scheme (Wild et al., 2000). Other major physical
107 parameterizations used in this study are listed in Table 1.

108 The initial and boundary meteorological conditions are provided by the National
109 Centers for Environmental Prediction (NCEP) Final Analysis data with a spatial
110 resolution of $1^\circ \times 1^\circ$. In order to limit the model bias of simulated meteorological fields,
111 the four-dimensional data assimilation (FDDA) is used with a nudging coefficient of
112 3.0×10^{-4} for the wind, temperature and humidity (no analysis nudging is applied for
113 the inner domain) (Lo et al., 2008; Otte, 2008). Chemical initial and boundary
114 conditions are obtained from the Model for Ozone and Related chemical Tracers,
115 version 4 (MOZART-4) forecasts (Emmons et al., 2010).

116 Anthropogenic emissions are taken from the 2010 MIX Asian emission inventory
117 (Li et al., 2017a), which provides emissions of sulfur dioxide (SO_2), nitrogen oxides
118 (NO_x), carbon monoxide (CO), non-methane volatile organic compounds (NMVOCs),
119 carbon dioxide (CO_2), ammonia (NH_3), black carbon (BC), organic carbon (OC), PM_{10}
120 (particulate matter with aerodynamic diameter is $10 \mu\text{m}$ and less) and $\text{PM}_{2.5}$. Emissions
121 are aggregated from four sectors, including power generation, industry, residential, and
122 transportation, with $0.25^\circ \times 0.25^\circ$ spatial resolution. Biogenic emissions are calculated
123 online by the Model of Emissions of Gases and Aerosols from Nature (MEGAN)
124 (Guenther et al., 2006).

125 **2.2 Numerical experiments**

126 To quantify the impacts of API and ARF on O_3 , three case simulations have been
127 conducted: (1) BASE – the base simulation coupled with the interactions between
128 aerosol and radiation, which includes both impacts of API and ARF; (2) NOAPI – the



129 same as the BASE case, but the impact of API is turned off (aerosol optical properties
130 are set to zero in the photolysis module), following Wu et al. (2020); (3) NOALL – both
131 the impacts of API and ARF are turned off (removing the mass of aerosol species
132 when calculating aerosol optical properties in the optical module), following Qiu et al.
133 (2017). The differences between BASE and NOAPI (i.e., BASE minus NOAPI)
134 represent the impacts of API. The contributions from ARF can be obtained by
135 comparing NOAPI and NOALL (i.e., NOAPI minus NOALL). The combined effects
136 of API and ARF on O₃ concentrations can be quantitatively evaluated by the differences
137 between BASE and NOALL (i.e., BASE minus NOALL).

138 Each simulation is conducted from 26 July to 3 August 2014, with the first 40 hours
139 as the model spin-up. Simulation results from the BASE case during 28 July and 3
140 August 2014 are used to evaluate the model performance.

141 **2.3 Observational data**

142 Simulation results are compared with meteorological and chemical measurements.
143 The surface-layer meteorological data (2 m temperature (T₂), 2 m relative humidity
144 (RH₂), and 10 m wind speed (WS₁₀)), with a temporal resolution of 3 h, at three stations
145 (Table S1) are obtained from NOAA's National Climatic Data Center
146 (<https://gis.ncdc.noaa.gov/maps/ncei/cdo/hourly>). The radiosonde data of temperature
147 at 08:00 and 20:00 LST in Beijing are provided by the University of Wyoming
148 (<http://weather.uwyo.edu/>). Observed hourly concentrations of PM_{2.5} and O₃ at thirty-
149 two sites (Table S2) in North China are collected from the China National
150 Environmental Monitoring Center (CNEMC). The photolysis rate of nitrogen dioxide
151 (NO₂) (J[NO₂]) measured at the Peking University site (39.99 °N, 116.31 °E) is also
152 used to evaluate the model performance. More details about the measurement technique
153 of J[NO₂] can be found in Wang et al. (2019).

154 **2.4 Integrated process rate analysis**

155 Integrated process rate (IPR) analysis has been widely used to quantify the
156 contributions of different processes to O₃ variations (Goncalves et al., 2009; Gao et al.,
157 2016b; Tang et al., 2017; Gao et al., 2018). In this study, four physical/chemical



158 processes are considered, including vertical mixing (VMIX), net chemical production
159 (CHEM), horizontal advection (ADVH), and vertical advection (ADVZ). VMIX is
160 initiated by turbulent process and closely related to PBL development, which influences
161 O₃ vertical gradients. CHEM represents the net O₃ chemical production (chemical
162 production minus chemical consumption). ADVH and ADVZ represent transport by
163 winds (Gao et al., 2016b). In this study, we define ADV as the sum of ADVH and ADVZ.

164 **3 Model evaluation**

165 Reasonable representation of observed meteorological and chemical variables by
166 the WRF-Chem model can provide foundation for evaluating the impacts of aerosols
167 on surface-layer ozone concentration. The model results presented in this section are
168 taken from the BASE case. The concentrations of air pollutants are averaged over the
169 thirty-two observation sites in Beijing, Tianjin and Baoding. To ensure the data quality,
170 the mean value for each time is calculated only when concentrations are available at
171 more than sixteen sites.

172 **3.1 Chemical simulations**

173 Figure 2 shows the spatial-temporal variations of observed and simulated PM_{2.5}
174 and O₃ concentrations over North China during 28 July to 3 August 2014. The observed
175 higher concentrations in Beijing and Baoding than those in Tianjin are well reproduced
176 by the WRF-Chem model. The model can also reasonably capture the temporal
177 variations of observed PM_{2.5} and O₃ with high correlation coefficients (R) of 0.66 for
178 PM_{2.5} and 0.86 for O₃, although simulated results underestimate the observed PM_{2.5} by
179 -19.2% and O₃ by -12.0%. The failure to reproduce PM_{2.5} peak values may be attributed
180 to incomplete treatments of chemical reactions in WRF-Chem, e.g., the aqueous-phase
181 reactions of SO₂ oxidized by NO₂ in aerosol water (Cheng et al., 2016). More statistical
182 parameters between simulations and observations are presented in Table 2.

183 **3.2 Meteorological simulations**

184 Figure 3 shows the time series of observed and simulated T₂, RH₂, and WS₁₀
185 averaged over three cities (Beijing, Tianjin, and Baoding), and J[NO₂] at Peking



186 University during 28 July to 3 August 2014. The statistical metrics for T_2 , RH_2 , WS_{10} ,
187 and $J[NO_2]$ are also presented in Table 2. Generally, the model can depict the temporal
188 variations of T_2 fairly well with R of 0.98 and the mean bias (MB) of -0.2 °C. For RH_2 ,
189 the R and MB are 0.93 and -6.0% , respectively. Although WRF-Chem model
190 overestimates WS_{10} with the MB of 0.6 $m\ s^{-1}$, the R for WS_{10} is 0.70 and the root-mean-
191 square error (RMSE) is 1.0 $m\ s^{-1}$, which is smaller than the threshold of model
192 performance criteria (2 $m\ s^{-1}$) proposed by Emery et al. (2001). The large positive bias
193 in wind speed was also reported in other studies (Zhang et al., 2010; Gao et al., 2015;
194 Liao et al., 2015; Qiu et al., 2017). The predicted $J[NO_2]$ agrees well with the
195 observations with R of 0.97 and NMB of 6.8%. We also conduct comparison between
196 observed and simulated temperature profiles at 08:00 and 20:00 LST in Beijing during
197 29 July to 1 August 2014 in Figure S1. The vertical profile of observed temperature,
198 especially the thermal inversion layer occurred on 31 July around 1600 m, is well
199 captured by the model. Generally, the WRF-Chem model reasonably reproduces the
200 temporal variations of observed meteorological parameters.

201 **4 Results**

202 It is known that co-occurrence of $PM_{2.5}$ and O_3 pollution is frequently observed
203 nowadays over China (Dai et al., 2021). The complex air pollution characterized by
204 high $PM_{2.5}$ and O_3 levels has already received widespread attentions from both
205 scientists and policy-makers. Therefore, we examine the impacts of aerosol-radiation
206 interactions on O_3 concentrations with a special focus on the complex air pollution areas
207 (CAPAs, Fig. S2), where the mean simulated daily $PM_{2.5}$ and MDA8 (maximum daily
208 8-h average) O_3 concentrations are larger than 75 $\mu g\ m^{-3}$ and 80 ppb, respectively, based
209 on the National Ambient Air Quality Standards (<http://www.mee.gov.cn>).

210 **4.1 Impacts of aerosol-radiation interactions on meteorology**

211 Figure 4 shows the impacts of aerosol-radiation interactions on downward
212 shortwave radiation at the surface (BOT_SW), downward shortwave radiation in the
213 atmosphere (ATM_SW), PBLH, T_2 , RH_2 , and WS_{10} during the daytime (08:00-17:00
214 LST) from 28 July to 3 August 2014. As a result of the interactions between aerosol and



215 radiation (the combined impacts of API and ARF), BOT_SW is decreased over the
216 entire simulated domain. Over CAPAs, the BOT_SW is decreased by 115.8 W m^{-2}
217 (20.5%). Contrary to the changes in BOT_SW, ATM_SW is increased significantly
218 with an increase of 72.8 W m^{-2} (25.3%) over CAPAs. The decreased BOT_SW perturbs
219 the near-surface energy flux, which weakens convection and suppresses the
220 development of PBL (Li et al., 2017b). The PBLH averaged over CAPAs is calculated
221 to decrease by 129.0 m (13.0%). The reduced surface radiation budget can directly lead
222 to changes in near-surface temperature. Therefore, the changes in T_2 have the similar
223 spatial patterns with BOT_SW; the surface temperature is decreased by $0.56 \text{ }^\circ\text{C}$
224 averaged over CAPAs. RH₂ is increased over most of the domain with an average rise
225 of 2.4%, which is beneficial for the hygroscopic growth of aerosols. WS₁₀ exhibits
226 overall reductions over CAPAs and is calculated to decrease by 0.12 m s^{-1} on average.
227 We also examine the changed meteorological variables caused by API and ARF
228 respectively. As shown in Fig. S3, API has little impact on meteorological variables;
229 the above changes are mainly caused by ARF.

230 **4.2 Impacts of aerosol-radiation interactions on photolysis**

231 Figure 5 shows the spatial distribution of mean daytime surface PM_{2.5}
232 concentrations simulated by BASE case and the changes in J[NO₂] and J[O¹D] due to
233 aerosol-radiation interactions from 28 July to 3 August 2014. When the combined
234 impacts (API and ARF) are considered, J[NO₂] and J[O¹D] are decreased over the entire
235 domain; the spatial patterns of changed J[NO₂] and J[O¹D] are similar to that of
236 simulated PM_{2.5}. The surface J[NO₂] and J[O¹D] are decreased by $1.8 \times 10^{-3} \text{ s}^{-1}$ (40.5%)
237 and $6.1 \times 10^{-6} \text{ s}^{-1}$ (48.8%) averaged over CAPAs. Figure S4 exhibits the percentage
238 changes in surface J[NO₂] and J[O¹D] caused by API and ARF respectively. It is found
239 that J[NO₂] and J[O¹D] are significantly modified by API and little affected by ARF.

240 **4.3 Impacts of aerosol-radiation interactions on O₃**

241 Figure 6 shows the changes in surface-layer O₃ due to API, ARF, and the combined
242 effects (denoted as ALL). As shown in Fig. 6a, API alone leads to overall O₃ decreases
243 over the entire domain with an average reduction of 8.5 ppb (10.1%) over CAPAs. The



244 change can be explained by the substantially diminished UV radiation due to aerosol
245 loading, which significantly weakens the efficiency of photochemical reactions and
246 restrains O₃ formation. The decreased surface O₃ concentration due to ARF, however,
247 is only 2.9 ppb (3.1%, Fig. 6b), which indicates that API is the dominant way for O₃
248 reduction related to aerosol-radiation interactions. The distributions of changed O₃
249 concentrations coincide with NO_x variations (Fig. S5b). Since North China is VOC-
250 limited (Jin et al., 2015), the increase in NO_x due to ARF may partly explain the O₃
251 decrease. The combined effects of API and ARF are shown in Fig. 6c. Generally,
252 aerosol-radiation interactions decrease the O₃ concentration by 11.4 ppb (13.5%)
253 averaged over CAPAs.

254 We further define an index to characterize the effects of aerosols on surface O₃
255 concentrations. The ratio of changes in O₃ to local PM_{2.5} levels is defined as:

$$256 \text{ ROP} = \frac{\Delta\text{O}_3}{\text{PM}_{2.5_}\text{BASE}},$$

257 where ΔO_3 is the changed O₃ concentration caused by ALL, and PM_{2.5}_BASE is the
258 surface PM_{2.5} concentration simulated in the BASE scenario. The calculated ROP is -
259 0.14 ppb (μg m⁻³)⁻¹ averaged over CAPAs, which means when the concentrations of
260 PM_{2.5} is 100 μg m⁻³, the O₃ decrease will be up to 14 ppb over CAPAs due to aerosol-
261 radiation interactions.

262 4.4 Influencing mechanism of aerosol-radiation interactions on O₃

263 Figure 7a shows diurnal variations of simulated surface daytime O₃ concentrations
264 over CAPAs in three cases (BASE, NOAPI, and NOALL). All cases present O₃
265 increases from 08:00 LST. It is shown that the simulated O₃ concentrations in BASE
266 case increase more slowly than that in NOAPI and NOALL cases. To explain the
267 underlying mechanisms of API and ARF impacts on O₃, we quantify the variations in
268 contributions of different processes (ADV, CHEM, and VMIX) to O₃ by using the IPR
269 analysis.

270 Figure 7b shows hourly surface O₃ changes induced by each physical/chemical
271 process (i.e., ADV, CHEM, and VMIX) in BASE case. The significant positive
272 contribution to the hourly variation in O₃ is contributed by VMIX, and the contribution



273 reaches the maximum at about 10:00 LST. After 14:00 LST, the contribution from
274 VMIX remains constant (nearly +2 ppb h⁻¹), which is probably attributed to the stable
275 boundary layer development (Tang et al., 2016). The CHEM process makes negative
276 contributions at around 09:00 and 16:00 LST, which means that the chemical
277 consumption of O₃ is stronger than the chemical production. At noon, the net chemical
278 contribution turns to be positive due to stronger solar UV radiation. The contribution
279 from all the processes (NET, the sum of VMIX, CHEM, and ADV) to O₃ is peaked at
280 the noon and then becomes weakened. After sunset (17:00 LST), the NET contribution
281 turns to be negative over CAPAs, leading to O₃ decrease.

282 Figure 7c shows the changes in hourly process contributions caused by API. The
283 chemical production of O₃ is suppressed significantly due to aerosol impacts on
284 photolysis rates. The weakened O₃ chemical production decreases the contribution from
285 CHEM, and results in a negative value of CHEM_DIF (-3.5 ppb h⁻¹). In contrast to
286 CHEM_DIF, the contribution from changed VMIX (VMIX_DIF) to O₃ concentration
287 due to API is always positive, and the mean value is +3.1 ppb h⁻¹. The impact of API
288 on ADV process is relatively small (-0.36 ppb h⁻¹). NET_DIF indicates the differences
289 in hourly O₃ changes caused by API. As shown in Fig. 7c, NET_DIF is almost negative
290 during the daytime over CAPAs with the mean value of -0.76 ppb h⁻¹. This is because
291 the decreases in CHEM and ADV are larger than the increases in VMIX caused by API;
292 the O₃ decrease is mainly attributed to the significantly decreased contribution from
293 CHEM. The maximum difference in O₃ between BASE and NOAPI appears at 17:00
294 LST with a value of -10.1 ppb (Fig. 7a).

295 Figure 7d shows the impacts of ARF on each physical/chemical process
296 contribution to the hourly O₃ variation. At 08:00 LST, the change in VMIX due to ARF
297 is large with a value of -4.6 ppb h⁻¹, resulting in a net negative variation with all
298 processes considered. The decrease in O₃ reaches the maximum with the value of 6.1
299 ppb at around 09:00 LST over CAPAs (Fig. 7a). During 10:00 to 16:00 LST, the positive
300 VMIX_DIF (mean value of +0.59 ppb h⁻¹) or the positive CHEM_DIF (mean value of
301 +0.16 ppb h⁻¹) is the major process to positive NET_DIF.

302 When both impacts of API and ARF are considered, the variation pattern of the



303 difference in hourly process contribution shown in Fig. 7e is similar to that in Fig. 7c,
304 which indicates that API is the dominant factor to O₃ reduction.

305 Figure 8 presents the vertical profiles of simulated daytime O₃ concentrations in
306 three cases (BASE, NOAPI, and NOALL), and the differences in contributions from
307 each physical/chemical process to hourly O₃ variations caused by API, ARF and the
308 combined effects during 28 July to 3 August 2014 over CAPAs. As shown in Fig. 8a,
309 the O₃ concentration is lower in BASE than that in other two scenarios (NOAPI and
310 NOALL), especially at the lower 12 levels, owing to the impacts of aerosols (API
311 and/or ARF).

312 The changes in each process contribution caused by API are presented in Fig. 8b.
313 The contribution from CHEM_DIF is -2.14 ppb h⁻¹ for first seven layers. Conversely,
314 the contribution from VMIX_DIF shows a positive value at the lower seven layers with
315 the mean value of +1.7 ppb h⁻¹. The positive variation in VMIX due to API may be
316 associated with the different vertical gradient of O₃ between BASE and NOAPI cases.
317 The contributions of changed advectations (ADVH_DIF and ADVZ_DIF) are relatively
318 small, with mean values of +0.25 and -0.47 ppb h⁻¹ respectively below the first seven
319 layers, which may result from small impact of API on wind filed (Fig. S3a). The net
320 difference is a negative value (-0.66 ppb h⁻¹); API leads to O₃ reduction not only nearly
321 surface but also in the aloft.

322 Figure 8c shows the differences in O₃ budget due to ARF. When the ARF is
323 considered, the vertical turbulence is weakened and the development of PBL is
324 inhibited, which makes VMIX_DIF negative at the lower 7 layers with a mean value of
325 -0.55 ppb h⁻¹, but the variation in CHEM caused by ARF is positive with a mean value
326 of +0.6 ppb h⁻¹. The chemical production of tropospheric O₃ is affected by both
327 photolysis rate and the concentrations of precursors (Tie et al., 2009). The enhanced O₃
328 precursors due to ARF can promote the chemical production of O₃. The changes of
329 ADVZ and ADVH (ADVZ_DIF and ADVH_DIF) caused by ARF are associated with
330 the variations in wind filed. When ARF is considered, the horizontal wind speed is
331 decreased (Fig. S6a), which makes ADVH_DIF positive at the lower twelve layers with
332 a mean value of +0.5 ppb h⁻¹. However, ADVZ_DIF is negative at these layers with a



333 mean value of -0.48 ppb h^{-1} because aerosol radiative effects decrease the transport of
334 O_3 from the upper to lower layers (Fig. S6b).

335 In Fig. 8d, the pattern and magnitude of the differences in process contributions
336 between BASE and NOALL are similar to those caused by API, indicating again the
337 dominate role of API on O_3 changes. The impacts of API on O_3 both near the surface
338 and aloft are greater than those of ARF.

339 5 Conclusions

340 In this study, the fully coupled regional chemistry transport model WRF-Chem is
341 applied to investigate the impacts of aerosol-radiation interactions, including the impact
342 of aerosol-photolysis interaction (API) and the impact of aerosol-radiation feedback
343 (ARF), on O_3 during a summertime complex air pollution episode from 28 July to 3
344 August 2014. Three sensitivity experiments are designed to quantify the respective and
345 combined impacts from API and ARF. Generally, the spatiotemporal distributions of
346 observed pollutant concentrations and meteorological parameters are captured fairly
347 well by the model with high correlation coefficients of 0.66–0.86 for pollutant
348 concentrations and 0.70–0.98 for meteorological parameters.

349 Sensitivity experiments show that aerosol-radiation interactions decrease
350 BOT_SW , T_2 , WS_{10} , PBLH , $\text{J}[\text{NO}_2]$, and $\text{J}[\text{O}^1\text{D}]$ by 115.8 W m^{-2} , $0.56 \text{ }^\circ\text{C}$, 0.12 m s^{-1} ,
351 129 m , $1.8 \times 10^{-3} \text{ s}^{-1}$, and $6.1 \times 10^{-6} \text{ s}^{-1}$ over CAPAs, and increase ATM_SW and RH_2
352 by 72.8 W m^{-2} and 2.4%. The changed meteorological variables and weakened
353 photochemistry reaction further reduce O_3 concentration by up to 11.4 ppb (13.5%),
354 with API and ARF contributing 74.6% and 25.4%, respectively. The combined impacts
355 of API and ARF on O_3 can be characterized by the ratio of changed O_3 (ΔO_3) to local
356 $\text{PM}_{2.5}$ level ($\text{PM}_{2.5_}\text{BASE}$), defining as $\text{ROP} = \Delta\text{O}_3/\text{PM}_{2.5_}\text{BASE}$. The calculated ROP
357 is $-0.14 \text{ ppb } (\mu\text{g m}^{-3})^{-1}$ averaged over CAPAs.

358 We further examine the influencing mechanism of aerosol-radiation interactions
359 on O_3 by using integrated process rate analysis. API can directly affect O_3 by reducing
360 the photochemistry reactions within the lower several hundred meters and therefore
361 amplify the O_3 vertical gradient, which promotes the contribution from VMIX and the



362 vertical mixing of O₃. The reduced photochemistry reactions of O₃ weaken the chemical
363 contribution and reduce surface O₃ concentrations, even though the enhanced vertical
364 mixing can partly counteract the reduction. ARF affects O₃ concentrations indirectly
365 through the changed meteorological variables, e.g., the decreased PBLH. The
366 suppressed PBL can weaken the vertical mixing of O₃ by turbulence. Generally, the
367 impacts of API on O₃ both near the surface and aloft are greater than those of ARF,
368 indicating the dominant role of API on O₃ reduction related with aerosol-radiation
369 interactions.

370 This study provides a detailed understanding of aerosol impacts on O₃ through
371 aerosol-radiation interactions (including both API and ARF). The results imply that
372 future PM_{2.5} reductions will lead to O₃ increases due to weakened aerosol-radiation
373 interactions. Recent study emphasized the need for controlling VOCs emissions to
374 mitigate O₃ pollution (Li et al., 2019). Therefore, tighter controls of O₃ precursors
375 (especially VOCs emissions) are needed to counteract future O₃ increases caused by
376 weakened aerosol-radiation interactions.



377 **Data availability**

378 The observed hourly surface concentrations of air pollutants are derived from the China
379 National Environmental Monitoring Center (<http://www.cnemc.cn>). The observed
380 surface meteorological data are obtained from NOAA's National Climatic Data Center
381 (<https://gis.ncdc.noaa.gov/maps/ncei/cdo/hourly>). The radiosonde data are provided by
382 the University of Wyoming (<http://weather.uwyo.edu/>). The photolysis rates of nitrogen
383 dioxide in Beijing are provided by Xin Li (li_xin@pku.edu.cn). The simulation results
384 can be accessed by contacting Lei Chen (chenlei@nuist.edu.cn) and Hong Liao
385 (hongliao@nuist.edu.cn).

386

387 **Author contributions**

388 HY, LC, and HL conceived the study and designed the experiments. HY and LC
389 performed the simulations and carried out the data analysis. JZ, WW, and XL provided
390 useful comments on the paper. HY prepared the paper with contributions from all co-
391 authors.

392

393 **Competing interests**

394 The authors declare that they have no competing interests.

395

396 **Acknowledgements**

397 This work is supported by the National Key R&D Program of China
398 (2019YFA0606804), the National Natural Science Foundation of China (42007195),
399 and the Meteorological Soft Science Program of China Meteorological Administration
400 (2021ZZXM46).



401 **Reference**

- 402 Albrecht, B. A.: Aerosols, cloud microphysics, and fractional cloudiness, *Science*, 245,
403 1227–1230, 1989.
- 404 Chen, F. and Dudhia, J.: Coupling an Advanced Land Surface – Hydrology Model with
405 the Penn State – NCAR MM5 Modeling System. Part I: Model Implementation and
406 Sensitivity, *Mon. Weather Rev.*, 129(4), 569–585, 2001.
- 407 Chen, L., Zhu, J., Liao, H., Gao, Y., Qiu, Y., Zhang, M., Liu, Z., Li, N., and Wang, Y.:
408 Assessing the formation and evolution mechanisms of severe haze pollution in the
409 Beijing–Tianjin–Hebei region using process analysis, *Atmos. Chem. Phys.*, 19,
410 10845–10864, <https://doi.org/10.5194/acp-19-10845-2019>, 2019.
- 411 Cheng, Y., Zheng, G., Chao, W., Mu, Q., Bo, Z., Wang, Z., Meng, G., Qiang, Z., He, K.,
412 and Carmichael, G.: Reactive nitrogen chemistry in aerosol water as a source of
413 sulfate during haze events in China, *Science Advances*, 2,
414 <https://doi.org/10.1126/sciadv.1601530>, 2016.
- 415 Dai, H., Zhu, J., Liao, H., Li, J., Liang, M., Yang, Y., and Yue, X.: Co-occurrence of
416 ozone and PM_{2.5} pollution in the Yangtze River Delta over 2013–2019:
417 Spatiotemporal distribution and meteorological conditions, *Atmos. Res.*, 249,
418 105363, 2021.
- 419 Dickerson, R. R., Kondragunta, S., Stenchikov, G., Civerolo, K. L., Doddridge, B. G.,
420 and Holben, B. N.: The impact of aerosols on solar ultraviolet radiation and
421 photochemical smog, *Science*, 278, 827–830, [10.1126/science.278.5339.827](https://doi.org/10.1126/science.278.5339.827), 1997.
- 422 Emery, C., Tai, E., and Yarwood, G.: Enhanced meteorological modeling and
423 performance evaluation for two Texas ozone episodes, in: Prepared for the Texas
424 Natural Resource Conservation Commission, ENVIRON International Corporation,
425 Novato, CA, USA, 2001.
- 426 Emmons, L. K., Walters, S., Hess, P. G., Lamarque, J.-F., Pfister, G. G., Fillmore, D.,
427 Granier, C., Guenther, A., Kinnison, D., Laepple, T., Orlando, J., Tie, X., Tyndall,
428 G., Wiedinmyer, C., Baughcum, S. L., and Kloster, S.: Description and evaluation of
429 the Model for Ozone and Related chemical Tracers, version 4 (MOZART-4), *Geosci.*



- 430 Model Dev., 3, 43–67, doi:10.5194/gmd-3-43-2010, 2010.
- 431 Foken, T.: 50 years of the Monin-Obukhov similarity theory, *Bound.-Layer Meteor.*,
432 119, 431–437, 2006.
- 433 Gao, J., Li, Y., Zhu, B., Hu, B., Wang, L., and Bao, F.: What have we missed when
434 studying the impact of aerosols on surface ozone via changing photolysis rates?,
435 *Atmos. Chem. Phys.*, 20, 10831–10844, [https://doi.org/10.5194/acp-20-10831-](https://doi.org/10.5194/acp-20-10831-2020)
436 2020, 2020.
- 437 Gao, J. H., Zhu, B., Xiao, H., Kang, H. Q., Pan, C., Wang, D. D., and Wang, H. L.:
438 Effects of black carbon and boundary layer interaction on surface ozone in Nanjing,
439 China, *Atmos. Chem. Phys.*, 18, 7081–7094, [https://doi.org/10.5194/acp-18-7081-](https://doi.org/10.5194/acp-18-7081-2018)
440 2018, 2018.
- 441 Gao, M., Carmichael, G. R., Wang, Y., Saide, P. E., Yu, M., Xin, J., Liu, Z., and Wang,
442 Z.: Modeling study of the 2010 regional haze event in the North China Plain, *Atmos.*
443 *Chem. Phys.*, 16, 1673–1691, doi:10.5194/acp-16-1673-2016, 2016a.
- 444 Gao, J., Zhu, B., Xiao, H., Kang, H., Hou, X., and Shao, P.: A case study of surface
445 ozone source apportionment during a high concentration episode, under frequent
446 shifting wind conditions over the Yangtze River Delta, China, *Sci. Total Environ.*,
447 544, 853, <https://doi.org/10.1016/j.scitotenv.2015.12.039>, 2016b.
- 448 Gao, Y., Zhang, M., Liu, Z., Wang, L., Wang, P., Xia, X., Tao, M., and Zhu, L.:
449 Modeling the feedback between aerosol and meteorological variables in the
450 atmospheric boundary layer during a severe fog–haze event over the North China
451 Plain, *Atmos. Chem. Phys.*, 15, 4279–4295, doi:10.5194/acp-15-4279-2015, 2015.
- 452 Goncalves, M., Jimenez-Guerrero, P., Baldasano, J.M.: Contribution of atmospheric
453 processes affecting the dynamics of air pollution in South-Western Europe during a
454 typical summertime photochemical episode, *Atmos. Chem. Phys.*, 9, 849 – 864,
455 doi:10.5194/acp-9-849-2009, 2009.
- 456 Grell, G. A., Peckham, S. E., Schmitz, R., Mckeen, S. A., Frost, G., Skamarock, K.,
457 and Eder, B.: Fully coupled “online” chemistry within the WRF model, *Atmos.*
458 *Environ.*, 39, 6957–6975, 2005.
- 459 Guenther, A., Karl, T., Harley, P., Wiedinmyer, C., Palmer, P. I., and Geron, C.:



- 460 Estimates of global terrestrial isoprene emissions using MEGAN (Model of
461 Emissions of Gases and Aerosols from Nature), *Atmos. Chem. Phys.*, 6, 3181–3210,
462 doi:10.5194/acp-6-3181-2006, 2006.
- 463 Hansen, J., Sato, M., and Ruedy, R.: Radiative forcing and climate response, *J. Geophys.*
464 *Res.*, 102, 6831–6864, 1997.
- 465 Haywood, J. and Boucher, O.: Estimates of the direct and indirect radiative forcing due
466 to tropospheric aerosols: A review, *Rev. Geophys.*, 38, 513–543, 2000.
- 467 Hong, S.-Y., Noh, Y., and Dudhia, J.: A New Vertical Diffusion Package with an
468 Explicit Treatment of Entrainment Processes, *Mon. Weather Rev.*, 134, 2318–2341,
469 2006.
- 470 Iacono, M. J., Delamere, J. S., Mlawer, E. J., Shephard, M. W., Clough, S. A., and
471 Collins, W. D.: Radiative forcing by long-lived greenhouse gases: Calculations with
472 the AER radiative transfer models, *J. Geophys. Res.*, 113, D13103,
473 doi:10.1029/2008JD009944, 2008.
- 474 Jin, X. and Holloway, T.: Spatial and temporal variability of ozone sensitivity over
475 China observed from the Ozone Monitoring Instrument, *J. Geophys. Res.-Atmos.*,
476 120, 7229–7246, <https://doi.org/10.1002/2015JD023250>, 2015.
- 477 Li, G., Bei, N., Tie, X., and Molina, L. T.: Aerosol effects on the photochemistry in
478 Mexico City during MCMA-2006/MILAGRO campaign, *Atmos Chem Phys*, 11,
479 5169-5182, 10.5194/acp-11-5169-2011, 2011.
- 480 Li, K., Jacob, D. J., Liao, H., Zhu, J., Shah, V., Shen, L., Bates, K. H., Zhang, Q., and
481 Zhai, S.: A two-pollutant strategy for improving ozone and particulate air quality in
482 China, *Nat. Geosci.*, 12, 906–910, <https://doi.org/10.1038/s41561-019-0464-x>, 2019.
- 483 Li, M., Zhang, Q., Kurokawa, J.-I., Woo, J.-H., He, K., Lu, Z., Ohara, T., Song, Y.,
484 Streets, D. G., Carmichael, G. R., Cheng, Y., Hong, C., Huo, H., Jiang, X., Kang, S.,
485 Liu, F., Su, H., and Zheng, B.: MIX: a mosaic Asian anthropogenic emission
486 inventory under the international collaboration framework of the MICS-Asia and
487 HTAP, *Atmos. Chem. Phys.*, 17, 935–963, <https://doi.org/10.5194/acp-17-935-2017>,
488 2017a.
- 489 Li, Z., Guo, J., Ding, A., Liao, H., Liu, J., Sun, Y., Wang, T., Xue, H., Zhang, H., and



- 490 Zhu, B.: Aerosol and boundary-layer interactions and impact on air quality, *Nat. Sci.*
491 *Rev.*, 4, 810–833, <https://doi.org/10.1093/nsr/nwx117>, 2017b.
- 492 Liao, H., Yung, Y. L., and Seinfeld, J. H.: Effects of aerosols on tropospheric photolysis
493 rates in clear and cloudy atmospheres, *J. Geophys. Res.*, 104, 23697–23707, 1999.
- 494 Liao, L., Lou, S. J., Fu, Y., Chang, W. Y., and Liao, H.: Radiative forcing of aerosols
495 and its impact on surface air temperature on the synoptic scale in eastern China [in
496 Chinese], *Chin. J. Atmos. Sci.*, 39, 68–82, doi: 10.3878/j.issn.1006-9895.1402.13302,
497 2015.
- 498 Lin, Y.-L., Farley, R. D., and Orville, H. D.: Bulk parameterization of the snow field in
499 a cloud model, *J. Clim. Appl. Meteorol.*, 22, 1065–1092, 1983.
- 500 Liu, Y. and Wang, T.: Worsening urban ozone pollution in China from 2013 to 2017 –
501 Part 1: The complex and varying roles of meteorology, *Atmos. Chem. Phys.*, 20,
502 6305–6321, <https://doi.org/10.5194/acp-20-6305-2020>, 2020.
- 503 Lo, J. C.-F., Yang, Z. L., and Pielke Sr, R. A.: Assessment of three dynamical climate
504 downscaling methods using the Weather Research and Forecasting (WRF) model, *J.*
505 *Geophys. Res.*, 113, D09112, doi:10.1029/2007jd009216, 2008.
- 506 Lohmann, U., and Feichter, J.: Global indirect aerosol effects: A review. *Atmospheric*
507 *Chemistry and Physics*, 5, 715–737, <https://doi.org/10.5194/acp-5-715-2005>, 2005.
- 508 Lou, S., Liao, H., and Zhu, B.: Impacts of aerosols on surface-layer ozone
509 concentrations in China through heterogeneous reactions and changes in photolysis
510 rates, *Atmos. Environ.*, 85, 123–138, 2014.
- 511 Miao, Y., Liu, S., Guo, J., Huang, S., Yan, Y., and Lou, M.: Unraveling the
512 relationships between boundary layer height and PM_{2.5} pollution in China based on
513 four-year radiosonde measurements, *Environmental Pollution*,
514 <https://doi.org/10.1016/j.envpol.2018.09.070>, 2018.
- 515 Otte, T. L.: The impact of nudging in the meteorological model for retrospective air
516 quality simulations. Part I: Evaluation against national observation networks. *J. Appl.*
517 *Meteor. Climatol.*, 47, 1853–1867, 2008.
- 518 Petäjä, T., Järvi, L., Kerminen, V. M., Ding, A. J., Sun, J. N., Nie, W., Kujansuu, J.,
519 Virkkula, A., Yang, X., Fu, C. B., Zilitinkevich, S., and Kulmala, M.: Enhanced air



- 520 pollution via aerosol-boundary layer feedback in China, *Sci. Rep.*, 6, 18998,
521 doi:10.1038/srep18998, 2016.
- 522 Qiu, Y., Liao, H., Zhang, R., and Hu, J.: Simulated impacts of direct radiative effects
523 of scattering and absorbing aerosols on surface layer aerosol concentrations in China
524 during a heavily polluted event in February 2014, *J. Geophys. Res. Atmos.*, 122,
525 5955–5975, doi:10.1002/2016JD026309, 2017.
- 526 Skamarock, W., Klemp, J. B., Dudhia, J., Gill, D. O., Barker, D. M., Duda, M., Huang,
527 X. Y., Wang, W., and Powers, J. G.: A description of the advanced research WRF
528 version 3, NCAR technical note NCAR/TN/u2013475, 2008.
- 529 Tang, G. Q., Zhu, X. W., Xin, J. Y., Hu, B., Song, T., Sun, Y., Zhang, J. Q., Wang, L. L.,
530 Cheng, M. T., Chao, N., Kong, L. B., Li, X., and Wang, Y. S.: Modelling study of
531 boundary-layer ozone over northern China – Part I: Ozone budget in summer, *Atmos.*
532 *Res.*, 187, 128–137, 2017.
- 533 Tang, G., Zhang, J., Zhu, X., Song, T., Munkel, C., Hu, B., Schäfer, K., Liu, Z., Zhang,
534 J., Wang, L., Xin, J., Suppan, P., and Wang, Y.: Mixing layer height and its
535 implications for air pollution over Beijing, China, *Atmos. Chem. Phys.*, 16, 2459–
536 2475, doi:10.5194/acp-16-2459-2016, 2016.
- 537 Tie, X., Geng, F., Li, P., Gao, W., and Zhao, C.: Measurement and modelling of ozone
538 variability in Shanghai, China, *Atmos. Environ.*, 43, 4289–4302, 2009.
- 539 Wang, W., Li, X., Shao, M., Hu, M., Zeng, L., Wu, Y., and Tan, T.: The impact of
540 aerosols on photolysis frequencies and ozone production in Beijing during the 4-year
541 period 2012–2015, *Atmos. Chem. Phys.*, 19, 9413–9429,
542 <https://doi.org/10.5194/acp19-9413-2019>, 2019.
- 543 Wild, O., Zhu, X., and Prather, M. J.: Fast-J: Accurate simulation of in- and below-
544 cloud photolysis in tropospheric chemical models, *J. Atmos. Chem.*, 37, 245–282,
545 doi:10.1023/A:1006415919030, 2000.
- 546 Wu, J., Bei, N., Hu, B., Liu, S., Wang, Y., Shen, Z., Li, X., Liu, L., Wang, R., Liu, Z.,
547 Cao, J., Tie, X., Molina, L. T., Li, G.: Aerosol-photolysis interaction reduces
548 particulate matter during wintertime haze events, *Proc. Natl. Acad. Sci. USA*, 117,
549 9755–9761, 2020.



- 550 Xing, J., Wang, J. D., Mathur, R., Wang, S. X., Sarwar, G., Pleim, J., Hogrefe, C.,
551 Zhang, Y. Q., Jiang, J. K., Wong, D. and Hao, J. M.: Impacts of aerosol direct effects
552 on tropospheric ozone through changes in atmospheric dynamics and photolysis rates,
553 *Atmos. Chem. Phys.*, 17, 9869–9883, <https://doi.org/10.5194/acp-17-9869-2017>,
554 2017.
- 555 Zaveri, R. A. and Peters, L. K.: A new lumped structure photochemical mechanism for
556 large-scale applications, *J. Geophys. Res.*, 104, D23, 30387–30415,
557 <https://doi.org/10.1029/1999JD900876>, 1999.
- 558 Zaveri, R. A., Easter, R. C., Fast, J. D., and Peters, L. K.: Model for simulating aerosol
559 interactions and chemistry (MOSAIC), *J. Geophys. Res.*, 113, D13204,
560 <https://doi.org/10.1029/2007JD008782>, 2008.
- 561 Zhang, X., Zhang, Q., Hong, C. P., Zheng, Y. X., Geng, G. N., Tong, D., Zhang, Y. X.,
562 and Zhang, X. Y.: Enhancement of PM_{2.5} concentrations by aerosol-meteorology
563 interactions over China. *Journal of Geophysical Research: Atmospheres*, 123, 1179–
564 1194, <https://doi.org/10.1002/2017JD027524>, 2018.
- 565 Zhang, Y., Wen, X.-Y., and Jang, C. J.: Simulating chemistry– aerosol–cloud–radiation–
566 climate feedbacks over the continental US using the online-coupled Weather
567 Research Forecasting Model with chemistry (WRF/Chem), *Atmos. Environ.*, 44,
568 3568–3582, doi:10.1016/j.atmosenv.2010.05.056, 2010.
- 569 Zhao, H.; Zheng, Y., and Li, C. Spatiotemporal distribution of PM_{2.5} and O₃ and their
570 interaction during the summer and winter seasons in Beijing, China. *Sustainability*,
571 10, 4519, 2018.
- 572 Zhu, J., Chen, L., Liao, H., and Dang, R.: Correlations between PM_{2.5} and Ozone over
573 China and Associated Underlying Reasons, *Atmosphere*, 352, 1–15,
574 <https://doi.org/10.3390/atmos10070352>, 2019.
- 575 Zhu, J., Chen, L., Liao, H., Yang, H., Yang, Y., and Yue, X.: Enhanced PM_{2.5} Decreases
576 and O₃ Increases in China During COVID-19 Lockdown by Aerosol-Radiation
577 Feedback, *Geophys. Res. Lett.*, 48, <https://doi.org/10.1029/2020GL090260>, 2021.
- 578



1 **Table 1.** Physical parameterization options used in the simulation.

Options	Schemes
Microphysics scheme	Lin (Purdue) scheme (Lin et al., 1983)
Cumulus scheme	Grell 3D ensemble scheme
Boundary layer scheme	Yonsei University PBL scheme (Hong et al., 2006)
Surface layer scheme	Monin-Obukhov surface scheme (Foken, 2006)
Land-surface scheme	Unified Noah land-surface model (Chen and Dudhia, 2001)
Longwave radiation scheme	RRTMG (Iacono et al., 2008)
Shortwave radiation scheme	RRTMG (Iacono et al., 2008)

2



1 **Table 2.** Statistical parameters between simulated and observed PM_{2.5} (μg m⁻³), O₃
 2 (ppb), 2 m temperature (T₂, °C), 2 m relative humidity (RH₂, %), 10 m wind speed
 3 (WS₁₀, m s⁻¹), and photolysis rate of NO₂ (J[NO₂], s⁻¹) during 28 July to 3 August 2014.

Variables	O ^a	M ^a	R ^b	MB ^c	ME ^d	NMB ^e (%)	NME ^f (%)	RMSE ^g
PM _{2.5}	113.3	90.7	0.66	-21.8	25.2	-19.2	22.2	30.1
O ₃	47.7	44.1	0.86	-5.7	15.5	-12.0	32.4	18.2
T ₂	28.4	28.0	0.98	-0.2	0.9	-0.7	3.3	1.1
RH ₂	70.9	65.7	0.93	-6.0	6.7	-8.5	9.5	8.7
WS ₁₀	2.4	3.0	0.70	0.6	0.9	27.9	36.6	1.0
J[NO ₂]	1.6×10 ⁻³	1.8×10 ⁻³	0.97	1.1×10 ⁻⁴	3×10 ⁻⁴	6.8	18.5	5.3×10 ⁻⁴

4 ^aO and M are the averages for observed and simulated results, respectively. O =

5 $\frac{1}{n} \times \sum_{i=1}^n O_i$, M = $\frac{1}{n} \times \sum_{i=1}^n M_i$.

6 ^bR is the correlation coefficient between observations and model results. R =

7
$$\frac{\sum_{i=1}^n (O_i - O) \times (M_i - M)}{\sqrt{\sum_{i=1}^n (O_i - O)^2 \times \sum_{i=1}^n (M_i - M)^2}}$$

8 ^cMB is the mean bias between observations and model results. MB = $\frac{1}{n} \times \sum_{i=1}^n (M_i -$
 9 O_i).

10 ^dME is the mean error between observations and model results. ME = $\frac{1}{n} \times \sum_{i=1}^n |M_i - O_i|$.

11 ^eNMB is the normalized mean bias between observations and model results. NMB =

12 $\frac{1}{n} \times \sum_{i=1}^n \frac{M_i - O_i}{O_i} \times 100\%$.

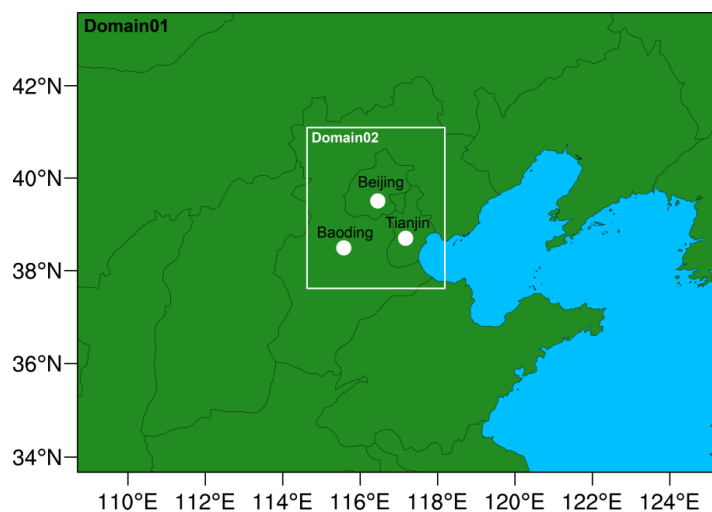
13 ^fNME is normal mean error between observations and model results. NME =

14 $\frac{1}{n} \times \sum_{i=1}^n \frac{|M_i - O_i|}{O_i} \times 100\%$.

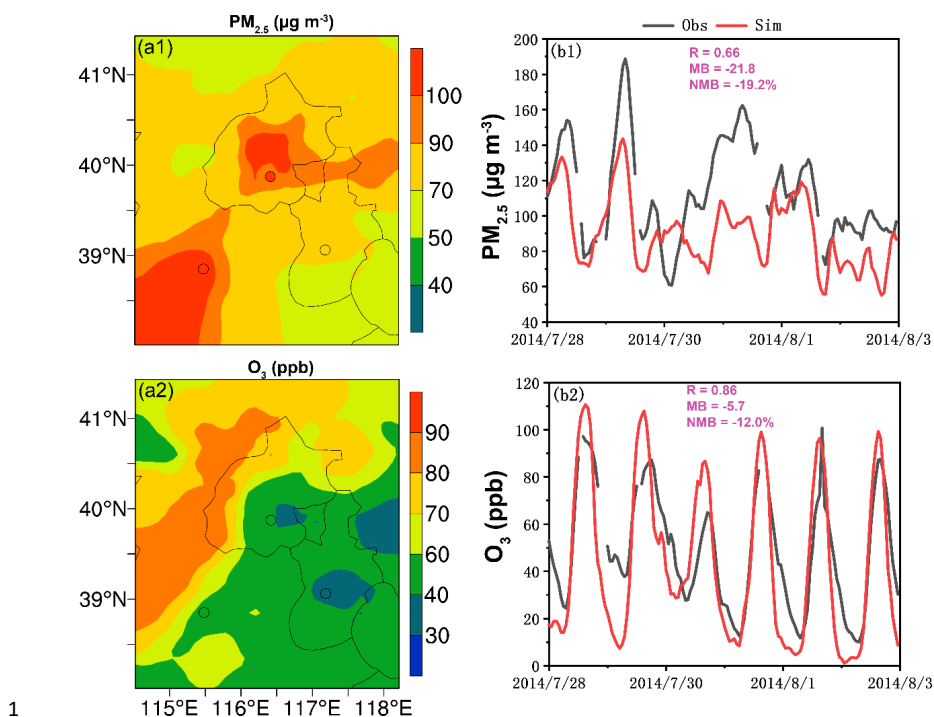
15 ^gRMSE is the root-mean-square error of observations and model results. RMSE =

16 $\sqrt{\frac{1}{n} \times \sum_{i=1}^n (M_i - O_i)^2}$.

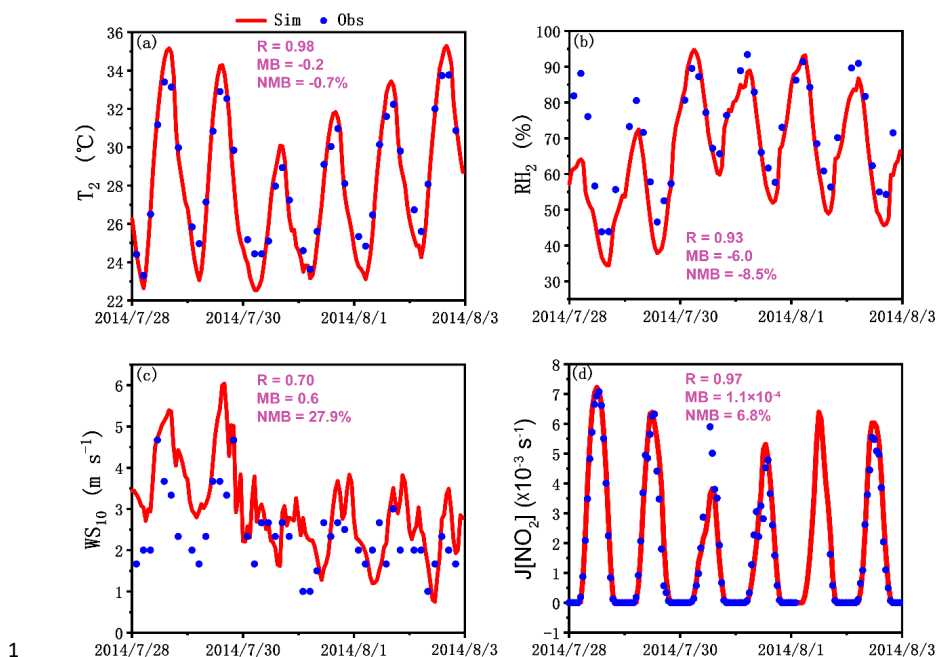
17 In the above O_i and M_i are the hourly observed and simulated data, respectively, and n
 18 is the total number of hours.



1
2 **Figure 1.** Map of the two WRF-Chem modeling domains and the locations of
3 observation sites (white dots) used for model evaluation.
4

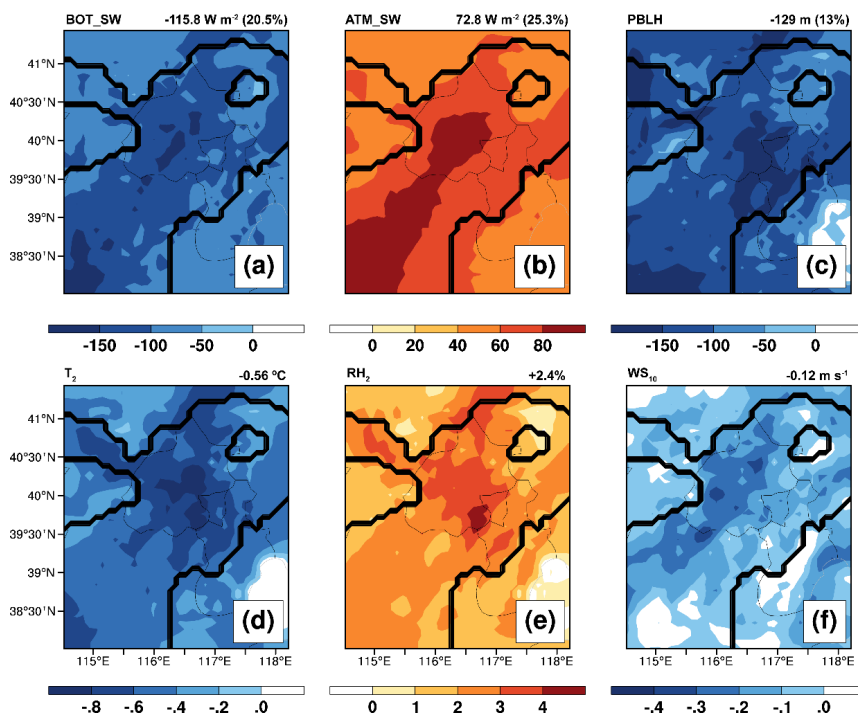


1
2 **Figure 2.** (a1-a2) Spatial distributions of simulated (color counters) and observed
3 (colored circles) $PM_{2.5}$ and O_3 concentrations averaged during 28 July to 3 August 2014.
4 (b1-b2) Time series of observed (black) and simulated (red) hourly $PM_{2.5}$ and O_3
5 concentrations averaged over the 32 observation sites in Beijing, Tianjin, and Baoding.
6 The calculated correlation coefficient (R), mean bias (MB), and normalized mean bias
7 (NMB) are also shown.
8



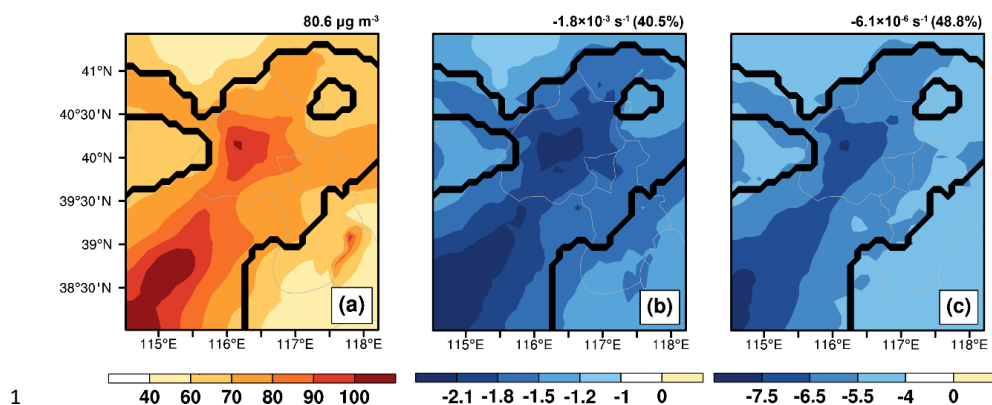
1
2 **Figure 3.** Time series of 3-hourly observed (blue dots) and hourly simulated (red lines)
3 (a) 2-m temperature (T_2), (b) 2-m relative humidity (RH_2), (c) wind speed at 10 m
4 (WS_{10}), and (d) surface photolysis rate of NO_2 ($J[\text{NO}_2]$) during 28 July to 3 August
5 2014. The calculated correlation coefficient (R), mean bias (MB), and normalized mean
6 bias (NMB) are also shown.

7

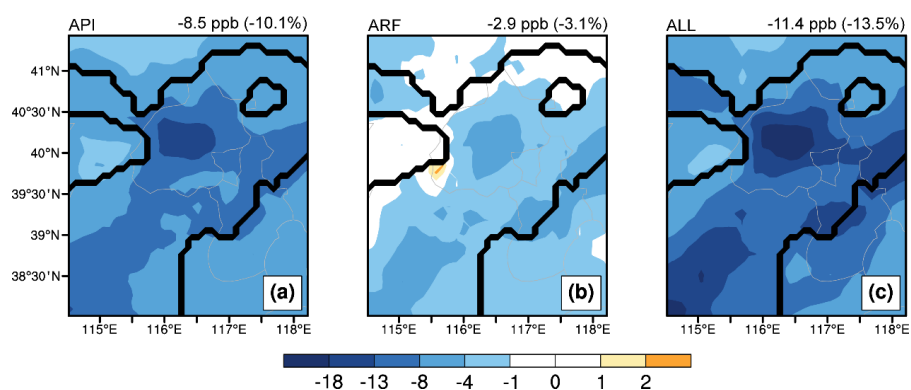


1
2
3
4
5
6
7
8
9
10

Figure 4. The impacts of aerosol-radiation interactions on (a) downward shortwave radiation at the surface (BOT_SW), (b) downward shortwave radiation in the atmosphere (ATM_SW), (c) PBL height (PBLH), (d) 2-m temperature (T_2), (e) 2-m relative humidity (RH_2), and (f) 10-m wind speed (WS_{10}) during the daytime (08:00-17:00 LST) from 28 July to 3 August 2014. The region sandwiched between two black lines is defined as the complex air pollution areas (CAPAs) where the mean daily $PM_{2.5}$ and MDA8 O_3 concentrations in BASE case are larger than $75 \mu g m^{-3}$ and 80 ppb. The calculated changes averaged over CAPAs are also shown at the top of each panel.



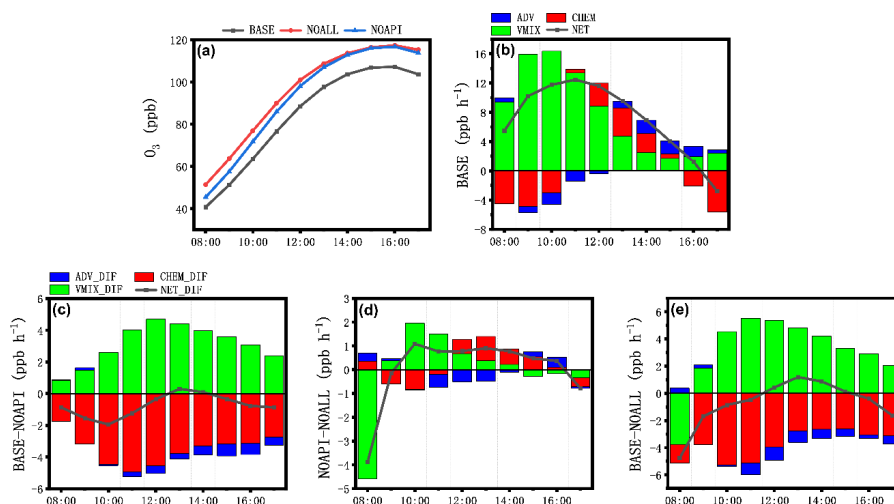
1
2 **Figure 5.** Spatial distributions of (a) simulated PM_{2.5} concentrations in BASE case, and
3 changes in (b) J[NO₂] and (c) J[O¹D] due to aerosol-radiation interactions during the
4 daytime (08:00-17:00 LST) from 28 July to 3 August 2014. The calculated values
5 (percentage changes) averaged over CAPAs are also shown at the top of each panel.



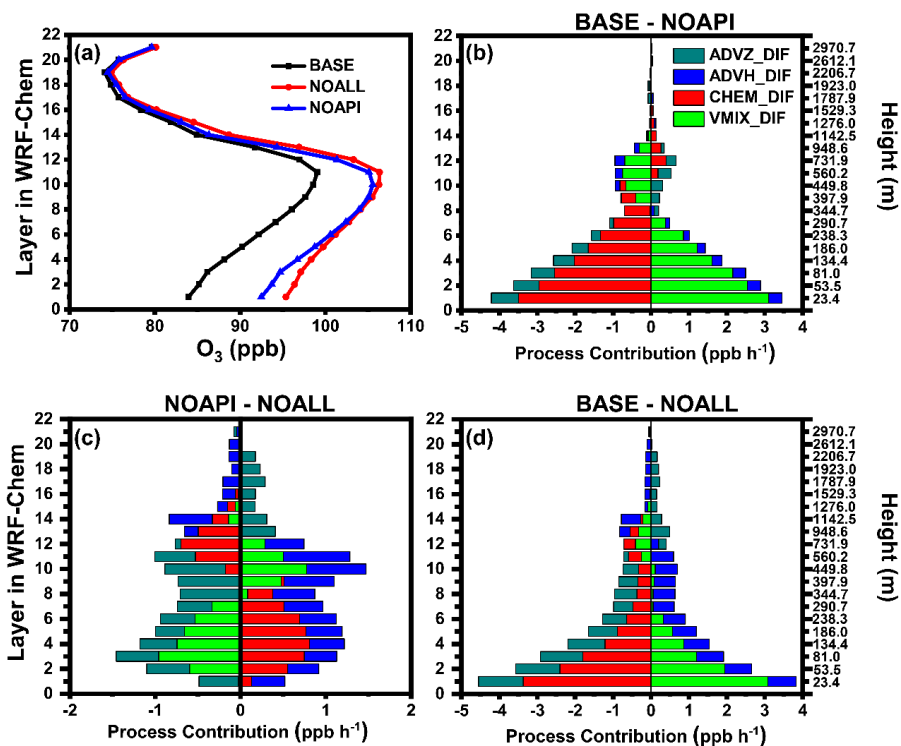
1

2 **Figure 6.** The changes in surface-layer ozone due to (a) aerosol-photolysis interaction
3 (API), (b) aerosol-radiation feedback (ARF), and (c) the combined effects (ALL,
4 defined as API+ARF) during the daytime (08:00-17:00 LST) from 28 July to 3 August
5 2014. The calculated mean changes averaged over CAPAs are also shown at the top of
6 each panel.

7



1
 2 **Figure 7.** (a) Diurnal variations of simulated O₃ concentrations in BASE (black),
 3 NOAPI (blue), and NOALL (red) cases over CAPAs. (b) The hourly O₃ changes
 4 induced by each physical/chemical process using the IPR analysis method in BASE
 5 case. (c-e) Changes in hourly O₃ process contributions caused by API (BASE minus
 6 NOAPI), ARF (NOAPI minus NOALL), and ALL (BASE minus NOALL) over CAPAs
 7 during the daytime (08:00-17:00 LST) from 28 July to 3 August 2014. The black lines
 8 with squares denote the net contribution of all processes (NET, defined as
 9 VMIX+CHEM+ADV). Differences of each process contribution are denoted as
 10 VMIX_DIF, CHEM_DIF, ADV_DIF, and NET_DIF.
 11



1

2 **Figure 8.** (a) Vertical profiles of simulated O₃ concentrations in BASE (black), NOAPI
 3 (blue), and NOALL (red) cases over CAPAs. (b-d) Changes in O₃ budget due to API,
 4 ARF, and ALL over CAPAs during the daytime (08:00-17:00 LST) from 28 July to 3
 5 August 2014. Differences of each process contribution are denoted by ADVZ_DIF,
 6 ADVH_DIF, CHEM_DIF, and VMIX_DIF.

7